

## **Chapter-2**

***Normal State Dynamical***

***Conductivity***

***of***

***Cuprate Superconductors***

## CHAPTER-II

### NORMAL STATE DYNAMICAL CONDUCTIVITY OF LAYERED SUPERCONDUCTORS

In this chapter, we performed a model calculation of normal state macroscopic and microscopic dynamical conductivity for layered superconductors which consists of one and two conducting layers per unit cell, in the long wave length limit. Our calculation incorporates; (i) weak tunnelling of current between the layers, (ii) strong electron-electron interactions which results in frequency and temperature dependent transport relaxation time and (iii) optical phonons which contribute to dynamical conductivity in infra-red frequency regime. Both  $a$ - $b$  plane and  $c$ -axis dynamical conductivity are calculated for longitudinal as well as transverse component of the field. It is found that both intralayer and interlayer interactions contribute to dynamical conductivity of a layered superconductor. Our computed macroscopic conductivity as a function of frequency and temperature shows good agreement with experimental results on  $\text{YBa}_2\text{Cu}_3\text{O}_7$ . In agreement with prior reported detailed numerical calculations, our model calculation of  $c$ -axis conductivity also shows a broad peak (which is attributed from tunnelling between layers) in infra-red frequency regime. We find that there exist one and two plasma modes, respectively in normal state of layered superconductors consisting of one and two conducting layers per unit cell, both in  $a$ - $b$  plane and along  $c$ -axis. On the other hand, several transverse electric modes are found to exist in a layered superconductor. One of the two plasma modes, in a layered superconductor

having two conducting layers per unit cell, is found to exist for wave vector values larger than critical value determined by intrinsic parameters of the superconductor. The complex frequency which describes a plasma mode or a transverse electric mode consists of large imaginary part as compared to its real part. The frequency and temperature dependent transport relaxation time which is needed to obtain a good agreement between theory and experiments, leads to larger imaginary part of complex frequency and the broad peaks in microscopic dynamical conductivity.

## 2.1 INTRODUCTION

The cuprate superconductors (CS) possess layered structure with extremely pronounced anisotropy. Intensive investigations have focused on how the layered structure of CS determines and affects their properties [1]. During early stage of investigations on CS, it was believed that their properties can be described in terms of the properties of two dimensional system, because of high anisotropy along  $c$ -axis. However, recent experimental as well as theoretical studies on CS reveal that there is an interaction between the layer, which gives rise to a possible charge transfer along  $c$ -axis [2-11]. The  $c$ -axis properties are found as important as  $a$ - $b$  plane properties in understanding the anomalous behavior of normal state and the mechanism of superconductivity in oxide cuprates. In fact, charge transport along  $c$ -axis of CS has been one of the mysteries of these materials. Measurements of conductivity in CS show that the electronic transport along  $c$ -axis is very different in character from the electronic transport in  $a$ - $b$  plane [2,3,6]. There have been speculation about the source of this difference. One school of thought believes that the unusual  $c$ -axis transport is due to a metallic ground state with some unconventional tunnelling between the layer, which gives rise to the charge transfer along  $c$ -axis [4-9]. It has also been claimed that unusual  $c$ -axis transport is evidence for some non-Fermi-

liquid like ground state with  $\text{CuO}_2$  layers. Recent angle-resolved photoemission [12] and time-resolved optical photomodulation [13] data suggest that some kind of gap may be present (at least for parts of Fermi surface) for charge excitations in underdoped CS. Measurement of  $c$ -axis frequency-dependent conductivity above  $T_c$  reveal a definite pseudogap in underdoped CS. Significant supercurrent along  $c$ -axis of underdoped  $\text{YBa}_2\text{Cu}_3\text{O}_{7.8}$  has also been observed which contradicts the idea of absence of coherence between different  $\text{CuO}_2$  layers in CS. Conductivity in  $a$ - $b$  plane has also been measured in different frequency ( $\omega$ ) and temperature ( $T$ ) regions. Optical conductivity data in  $a$ - $b$  plane have so far mainly been discussed in terms of an extended Drude model with  $\omega$ -and  $T$ -dependent scattering relaxation time,  $\tau(\omega, T)$  and charge carrier effective mass  $m^*(\omega, T)$  [14,15]. The  $a$ - $b$  plane normal state conductivity exhibits larger spectral weight at high frequency than would be present from a Drude formula with  $\omega$ -dependent  $\tau(\omega, T)$ . It has been suggested that this behavior reflects a two component charge carrier picture above a certain crossover temperature [16]. Other special features in conductivity of CS are; (i) similarity in the  $\omega$ -dependent behavior of conductivity in microwave and infra-red region below and above  $T_c$  and (ii) a broad peak in temperature dependent microwave conductivity.

Another important aspect, which involves the dynamical conductivity of a system, is propagation of electromagnetic (EM) waves. There have been several experimental and theoretical studies on plasmons in normal state of CS [17-20]. Proposed mechanism of superconductivity via exchange of plasmons has motivated the study of plasmons in CS. Propagation of transverse electromagnetic (TEM) and longitudinal electromagnetic (LEM) modes have been studied theoretically in metallic superlattices which have been taken as a model for high  $T_c$  superconductors [21]. It was concluded that the photon line

separates the TEM and LEM modes in a metallic superlattices and a single 2D metallic sheet cannot support the propagation of TEM modes.

The aim of this chapter is to understand some of basic aspects of normal state conductivity in a simple manner. Our simple model calculation of normal state conductivity take into account weak coupling between the conducting  $\text{CuO}_2$  layers in order to allow charge transport along  $c$ -axis. It also uses  $\omega$ -and  $T$ -dependent  $\tau$ . We calculate macroscopic and microscopic longitudinal and transverse conductivities in normal state of CS consisting of one and two conducting layers per unit cell. Frequencies of longitudinal electronic collective excitations (plasmons) and of transverse electronic collective excitations (also known as transverse electric) modes are calculated from microscopic conductivity. The macroscopic conductivity is expressed in terms of bare susceptibility and it relates the current density to macroscopic field. Whereas, microscopic conductivity is expressed in terms of screened susceptibility and it correlates current density to externally applied field. Our calculation is applied to  $\text{La}_{2-x}\text{Sr}_x\text{CuO}_4$  (LSCO) and  $\text{YBa}_2\text{Cu}_3\text{O}_7$  (YBCO) by modelling them as a layered structure with one and two conducting  $\text{CuO}_2$  layer per unit cell, respectively. Tunnelling between conducting layers is taken into account through single particle energy and Coulomb potential. A tight binding type energy dispersion allows the possible charge transfer between the layers. It is further assumed that conducting layers are embedded into an anisotropic dielectric host medium. The contribution of lattice vibrations to dynamical conductivity is incorporated through a phenomenological background dielectric function. The frequency of lattice vibrations along  $a$ - $b$  plane and along  $c$ -axis are taken to be different. It is found that the frequency of an electronic collective excitation mode along  $a$ - $b$  plane is much higher than that along  $c$ -axis. The soft electronic collective excitation modes exist along  $c$ -axis, whose frequencies are comparable to those of optical phonons. Our calculations of longitudinal and

transverse conductivity and polarizability are given in section-2.2. The d. c. conductivity is described in section-2.3. Conductivity along *a-b* plane and along *c*-axis are given in sections 2.4 and 2.5, respectively.

## 2.2 LONGITUDINAL AND TRANSVERSE CONDUCTIVITIES

Application of an electromagnetic field produces induced charge and current densities in a system. On combining Maxwell's equations with equation of continuity, dynamical longitudinal and transverse conductivities are given by [22,23]

$$\sigma_L(\mathbf{r}, \mathbf{r}', \omega) = \int [\epsilon_L(\mathbf{r}, \mathbf{r}'', \omega)]^{-1} \sigma_L^0(\mathbf{r}'', \mathbf{r}', \omega) d^3 \mathbf{r}'' \quad (2.1)$$

and

$$\sigma_T(\mathbf{r}, \mathbf{r}', \omega) = \int F^1(\mathbf{r}, \mathbf{r}'', \omega) \sigma_T^0(\mathbf{r}'', \mathbf{r}', \omega) d^3 \mathbf{r}''. \quad (2.2)$$

The  $\sigma_L$  ( $\sigma_T$ ) is longitudinal (transverse) microscopic quasi-conductivity, whereas  $\sigma_L^0$  ( $\sigma_T^0$ ) is macroscopic longitudinal (transverse) conductivity.  $\epsilon_L(\mathbf{r}, \mathbf{r}', \omega)$  and  $F(\mathbf{r}, \mathbf{r}', \omega)$  are response functions for longitudinal and transverse fields, respectively. The  $F(\mathbf{r}, \mathbf{r}', \omega)$  is defined as [22]

$$F(\mathbf{r}, \mathbf{r}', \omega) = \delta(\mathbf{r} - \mathbf{r}') - \{i\omega/c^2\} [G(\mathbf{r}, \mathbf{r}'', \omega) \sigma_T^0(\mathbf{r}'', \mathbf{r}', \omega) d^3 \mathbf{r}'', \quad (2.3)$$

where *c* is velocity of light and

$$G(\mathbf{r}, \mathbf{r}', \omega) = \frac{\exp\{ik|\mathbf{r} - \mathbf{r}'|\}}{|\mathbf{r} - \mathbf{r}'|} \quad (2.4)$$

is proper Green function and  $k = \omega/c$ . In non-retarding limit, which is of our interest for longitudinal field,  $\epsilon_L(\mathbf{r}, \mathbf{r}', \omega)$  is given by [23]

$$\epsilon_L(\mathbf{r}, \mathbf{r}', \omega) = \epsilon_l(\omega) \delta(\mathbf{r} - \mathbf{r}') - \int \alpha_L(\mathbf{r}, \mathbf{r}'', \omega) v(\mathbf{r}'', \mathbf{r}') d^3\mathbf{r}'', \quad (2.5)$$

where  $\alpha_L(\alpha_T)$  is polarization response function for longitudinal (transverse) field in absence of bare Coulomb electron-electron interaction

$$v(\mathbf{r}, \mathbf{r}') = \frac{e^2}{|\mathbf{r} - \mathbf{r}'|} \quad (2.6)$$

$\epsilon_l(\omega)$  is the lattice dielectric function which consists of lattice vibrational frequencies. Existing theoretical and experimental investigations suggest that there are several optical and acoustic phonon branches in CS [24]. In this study of conductivity, our focus is on electronic transitions in CS. We therefore take into account only the optical phonon to express  $\epsilon_l(\omega)$  in following simple form;

$$\epsilon_l(\omega) = \epsilon_\infty / l \sum_{i=1}^l \frac{[\omega_{Li}^2 - \omega(\omega + i\gamma_{ph})]}{[\omega_{Ti}^2 - \omega(\omega + i\gamma_{ph})]} \quad (2.7)$$

The  $\epsilon_\infty$  is high frequency dielectric constant. The  $\omega_{Li}$  ( $\omega_{Ti}$ ) is the longitudinal (transverse) phonon frequency of  $i^{\text{th}}$  branch.  $\gamma_{ph}$  is the damping constant for lattice vibrations, which is taken same for all phonon branches. We assumed that our model CS is a one-dimensional (1D) periodic sequence of two-dimensional

(2D) conducting planes (2DCP) embedded in a dielectric host medium represented by  $\epsilon_l(\omega)$ . The  $a$ - $b$  plane of our model CS is taken along  $x$ - $y$  plane, whereas  $c$ -axis is taken along  $z$ -axis. The length of unit cell is denoted by  $d$ . We Fourier transform Eqs. (2.1) and (2.2) using continuous transformation in  $x$ - $y$  plane and a discrete transformation along  $z$ -axis to obtain

$$\sigma_{mL}(\mathbf{q}, k_z, \omega, T) = \frac{\sigma_{mL}^0(\mathbf{q}, k_z, \omega, T)}{\epsilon_m(\mathbf{q}, k_z, \omega, T)} \quad (2.8)$$

and

$$\sigma_{mT}(\mathbf{q}, k_z, \omega, T) = \frac{\sigma_{mT}^0(\mathbf{q}, k_z, \omega, T)}{F_m(\mathbf{q}, k_z, \omega, T)} \quad (2.9)$$

where index  $m$  takes value 1 and 2 for CS consisting of one 2DCP and two 2DCP per unit cell, respectively.

$$\sigma_{LT}^0(\mathbf{q}, k_z, \omega, T) = \{-i\omega/4\pi\}[\epsilon_{LT}(\mathbf{q}, k_z, \omega, T) - 1] \quad (2.10)$$

$$\epsilon_l(\mathbf{q}, k_z, \omega, T) = \epsilon_L(\mathbf{q}, k_z, \omega, T) \quad (2.11)$$

$$F_l(\mathbf{q}, k_z, \omega, T) = 1 - \{\omega(\omega+i\gamma)d/2pc^2\}S(\mathbf{p}, k_z)\{\epsilon_T(\mathbf{q}, k_z, \omega, T) - 1\} \quad (2.12)$$

where  $\mathbf{q}$  and  $k_z$  are wave vector components along  $a$ - $b$  plane and  $c$ -axis, respectively. The  $S(\mathbf{p}, k_z)$  and  $\epsilon_{LT}(\mathbf{q}, k_z, \omega, T)$  are defined as

$$S(\mathbf{p}, k_z) = \frac{\sinh(pd)}{\cosh(pd) - \cos(k_z d)} \quad (2.13)$$

$$\epsilon_{LT}(q, k_z, \omega, T) = \epsilon_1(\omega) - \{2\pi e^2 d/q\} \alpha_{LT}(q, k_z, \omega, T) S(q, k_z) \quad (2.14)$$

Here,  $p = [q^2 - \omega^2/c^2]^{1/2}$  for  $qc > \omega$  and  $p = -i[\omega^2/c^2 - q^2]^{1/2}$  for  $qc < \omega$ .  $S(q, k_z)$  is obtained from Eq.(2.13) on replacing  $p$  by  $q$ . For CS consisting of two 2DCP per unit cell, we obtain

$$\begin{aligned} \sigma_{2L}^0(q, k_z, \omega, T) = \\ \sigma_{1L}^0(q, k_z, \omega, T) [2 - \{2\pi e^2 d/q\} \alpha_L(q, \omega, T) \{2S(q, k_z) - S'(q, k_z) - S''(q, k_z)\}] \end{aligned} \quad (2.15)$$

$$\begin{aligned} \epsilon_2(q, k_z, \omega, T) = \epsilon_1(\omega) - [\{4\pi e^2 d/q\} \alpha_L(q, k_z, \omega, T) S(q, k_z)] \\ + [\{2\pi e^2 d/q\}^2 / \epsilon_1(\omega)] \alpha_L^2(q, k_z, \omega, T) \{S^2(q, k_z) - S'(q, k_z) S''(q, k_z)\} \end{aligned} \quad (2.16)$$

$$\begin{aligned} \sigma_{2T}^0(q, k_z, \omega, T) = \\ \sigma_{1T}^0(q, k_z, \omega, T) [2 - \{2\pi i \omega d/p c^2\} \sigma_{1T}^0(q, k_z, \omega, T) \{2S(q, k_z) - S'(q, k_z) - S''(q, k_z)\}] \end{aligned} \quad (2.17)$$

$$\begin{aligned} F_2(q, k_z, \omega, T) = \\ [1 - \{\omega(\omega + i\gamma)d/p c^2\} \{\epsilon_T(q, k_z, \omega, T) - 1\} S(p, k_z)] \\ + [\{\omega(\omega + i\gamma)/2p c^2\} \{\epsilon_T(q, k_z, \omega, T) - 1\}]^2 [S^2(p, k_z) - S'(p, k_z) S''(p, k_z)] \end{aligned} \quad (2.18)$$

The  $S'(p, k_z)$  is defined as

$$S'(p, k_z) = \frac{\sinh(pd') + \exp(-ik_z d)\sinh(pd_1)}{\cosh(pd) - \cos(k_z d)} \quad (2.19)$$

where  $d' = d - d_1$ ,  $d_1$  is separation between two 2DCP in a unit cell of CS consisting of two 2DCP per unit cell. The  $S''(p, k_z)$  is complex conjugate of  $S'(p, k_z)$ .  $S'(q, k_z)$  and  $S''(q, k_z)$  are obtained from  $S'(p, k_z)$  and  $S''(p, k_z)$ , respectively on replacing  $p$  by  $q$ . In obtaining Eqs. (2.12) to (2.14), we have considered a weak coupling between 2DCP. In case of CS, conducting layer consisting of electrons is much smaller than the separation between the layers. Therefore, there is a small transfer of charge between conducting layers. Possible charge transfer between conducting layers of a CS is also to be introduced in  $\alpha_{L/T}(q, k_z, \omega, T)$  through single particle energy involving half width of a miniband ( $W$ ) and the wave functions [25,26]. In order to understand, in a simple manner, the experimental results on electromagnetic response of a CS, we restrict ourselves to long wave length limit of  $\alpha_{L/T}(q, k_z, \omega, T)$ . In long wave length limit,  $\alpha_L = \alpha_T$ . For weak coupling case ( $W \ll E_F$ ,  $E_F$  being Fermi energy of 2D surface) a simple form of  $\alpha_{L/T}(q, k_z, \omega, T)$  in long wave length limit can be given by [26,27]

$$\alpha_{L/T}(q, k_z, \omega, T) = \left[ \frac{nq^2}{m^* \omega(\omega + i\gamma)} \right] \left[ 1 + \frac{4\omega_g^2 \sin^2(k_z d/2)}{\omega_p^2 (qd)^2} \right], \quad (2.20)$$

where  $\omega_p = \{4\pi n e^2 / m^*\}^{1/2}$  is usual plasma frequency. The  $n$  is number of electrons per unit volume and  $\gamma$  is damping constant for electronic transitions. The  $\gamma$  has

been found  $\omega$  and  $T$  dependent in CS. A simple expression, which very well describes asymptotic behavior of  $\gamma$  in CS, is given as [28]

$$\gamma = \delta [\beta^2 + \omega^2]^{1/2} \quad (2.21)$$

where  $\delta$  and  $\beta$  are the constants which depends on nature of electron-electron interaction in CS.  $\delta$  is independent on  $T$ , whereas  $\beta$  depend on  $T$ .  $\omega_g$  depends upon  $d$ , the effective Bohr's radius  $a^* = \hbar^2/m^* e^2$  and overlap integral between the wave functions of adjacent layers (i.e.  $W$ ). In case of very small overlap of wave functions on adjacent layers (weak coupling,  $2W \ll E_F$ , as is the case for CS),  $\omega_g$  is approximately given by [25]

$$\hbar\omega_g = W\{2d/a^*\}^{1/2}. \quad (2.22)$$

The  $\omega_g$  does not appear in single particle energy but it appears in  $\alpha_{L/T}(q, k_z, \omega, T)$ . Therefore, it represents a pseudogap whose presence at Fermi surface has been suggested by angle-resolved photoemission [12] and time-resolved optical modulation [13] experiments. The  $\sigma_{IL}(q, k_z, \omega, T)$  exhibits peak for  $\omega$  close to  $\omega_{IL}(q, k_z)$  which is given by the real part of zero of  $\epsilon(q, k_z, \omega, T)$ .  $\omega_{IL}(q, k_z)$  is the frequency of plasma oscillations. Computation of  $\omega_{IL}(q, k_z)$  as a function of  $q$  for  $-1 < \cos(k_z d) < 1$  gives rise to a full band of plasma frequencies. The lower edge of the band, which occurs for  $\cos(k_z d) = -1$  approaches to  $\omega_g\{1/2(1/\Delta_c - 1/\Delta_c^2)\}^{1/2}$ , whereas upper edge goes to  $\omega_p\{1/2(1/\Delta_{ab} - 1/\Delta_{ab}^2)\}^{1/2}$ , where  $\Delta_{ab} = \{1 + \delta_{ab}^2\}^{1/2}$  and  $\Delta_c = \{1 + \delta_c^2\}^{1/2}$  for  $q \rightarrow 0$ .  $\delta_{ab}(\beta_{ab})$  and  $\delta_c(\beta_c)$  are the values of  $\delta(\beta)$  along  $a$ - $b$  plane and along  $c$ -axis, respectively. The  $\delta_{ab}(\beta_{ab})$  and  $\delta_c(\beta_c)$  differ from each other because of the difference in strength of electron-electron interaction along  $a$ - $b$  plane and along  $c$ -axis. Also, the  $T$ -dependence of  $\beta_{ab}$  and  $\beta_c$  are different.  $\gamma$  is roughly proportional to  $\omega$  at higher  $\omega$ -values. As has

been discussed at several places in existing literature, tunnelling between layers introduced an energy gap at lower part of plasma spectrum of a superlattices [26,27]. Therefore a superlattice structure with tunnelling between layers can not support acoustic plasmons, for  $qd \ll 1$ .

### 2.3. THE D.C. CONDUCTIVITY

The deduced d. c. conductivity from our formalism, we take  $qd \rightarrow 0$  and  $k_z d \rightarrow 0$  limit of Eqs. (2.10) and (2.15). For  $qd \rightarrow 0$ , both  $\sigma_{2L}^0(q, k_z)$  and  $\sigma_{2T}^0(q, k_z)$  reduces to  $2\sigma_{1L}^0(q, k_z)$  as can be seen from Eqs. (2.15) and (2.17). From Eq. (2.10), we obtain

$$\sigma_d(q, k_z, \omega, T) = \left\{ \frac{ne^2}{m^* \gamma} \right\} \left\{ \frac{q^2 + (\omega_g^2 / \omega_P^2) k_z^2}{(q^2 + k_z^2)} \right\} + \{-i\omega/4\pi\} \{\epsilon_1(\omega) - 1\}. \quad (2.23)$$

The d.c. conductivity in  $a$ - $b$  plane ( $k_z d = 0$ ) is

$$\sigma_d^{ab} = \left\{ \frac{ne^2}{m^* \delta_{ab} \beta_{ab}} \right\}, \quad (2.24)$$

whereas d.c. conductivity along  $c$ -axis is obtained by putting  $q = 0$  in Eq. (2.23)

$$\sigma_d^c = \left\{ \frac{\omega_g^2}{4\pi \delta_c \beta_c} \right\}. \quad (2.25)$$

Equation (2.24) and (2.25) are used to determine  $T$ -dependent of  $\beta_{ab}$  and  $\beta_c$ . Experimental measurements on  $\rho_{ab}$  and  $\rho_c$  as a function of  $T$  suggest that one can take  $\beta_{ab} = \lambda_{ab} T$  and  $\beta_c = \lambda_c / T$ , where  $\lambda_{ab}$  and  $\lambda_c$  are independent of  $T$

and  $\omega$  [29]. The anisotropy ratio of resistivity ( $\rho_c/\rho_{ab}$ ), using (2.24) and (2.25) is given by

$$\rho_c/\rho_{ab} = \{\omega_g^2/\omega_p^2\}\{\delta_{ab}\lambda_{ab}/\delta_c\lambda_c\}T^2 \quad (2.26)$$

Equation (2.26) can be used to estimate  $\omega_g\{\delta_{ab}\lambda_{ab}/\delta_c\lambda_c\}^{1/2}$  by using experimentally measured value of ( $\rho_c/\rho_{ab}$ ) and  $\omega_p$  at given T-value. ( $\rho_c/\rho_{ab}$ ) has been found reasonably high for CS. One can take ( $\rho_c/\rho_{ab}$ ) = 150 for LSCO at T=40K and ( $\rho_c/\rho_{ab}$ ) = 200 for YBCO at T=100K [29]. The electron-electron interaction within *a-b* plane is stronger than that along *c*-axis.  $\gamma$ , in our calculation, is a measure of strength of electron-electron interaction. This suggests that  $\gamma_{ab} > \gamma_c$  at given values of  $\omega$  and T. Further,  $\omega_g$  which is the measure of coupling between conducting layers, should be smaller than  $\omega_p$ . In view of this, we choose  $\gamma_{ab}/\gamma_c = 5.0$  at  $\omega=0$ . As  $\rho_c$  is high yet never infinite, our Eq. (2.26) justifies the existence of  $\omega_g$  in CS. This can be taken as an experimental evidence for charge transfer along *c*-axis in CS.

#### 2.4. CONDUCTIVITY IN *a-b* PLANE

The *a-b* plane conductivities are calculated by substituting Eqs. (2.20) and (2.21) into Eq. (2.10) and (2.15) and then taking  $k_z d \rightarrow 0$  limit of Eqs. (2.8) to (2.19). Equation (2.20) for *a-b* plane conduction, reduces to

$$\alpha^{ab}(q, \omega, T) = \frac{nq^2}{m^* \omega(\omega + i\gamma_{ab})} \quad (2.27)$$

LSCO is modelled as CS consisting of one 2DCP per unit cell in terms of following value of parameter:  $\omega_p=1.308$  eV,  $\omega_g=0.238$  eV,  $\epsilon_\infty=5.0$ ,  $\delta_{ab}=0.55$ ,  $\lambda_{ab}=0.80$  meV/K and  $d=13.25$  Å<sup>0</sup>. To model YBCO as a CS with two 2DCP per unit cell, we take  $\omega_p=1.315$  eV and  $\omega_g=0.239$  eV,  $\epsilon_\infty=4.0$ ,  $\delta_{ab}=0.55$ ,  $\lambda_{ab}=0.4$  meV/K,  $d=11.67$  Å<sup>0</sup> and  $d_I=d/3$ . The  $\gamma_{ab}$  is given by Eq. (2.21) on replacing  $\delta$  by  $\delta_{ab}$  and  $\beta$  by  $\lambda_{ab}T$ . To compute  $\epsilon_i(\omega)$  for  $a$ - $b$  plane,  $\epsilon_i^{ab}(\omega)$ , for LSCO and YBCO, we used calculated optical phonon frequencies reported by Parade et.al.[24]. The reported values for LSCO are;  $\omega_{L1}=81.80$  meV,  $\omega_{L2}=48.37$  meV,  $\omega_{L3}=18.69$  meV,  $\omega_{T1}=80.56$  meV,  $\omega_{T2}=44.62$  meV and  $\omega_{T3}=16.73$  meV. And, for YBCO  $\omega_{L1}=67.35$  meV,  $\omega_{L2}=58.25$  meV,  $\omega_{L3}=42.38$  meV,  $\omega_{L4}=29.62$  meV,  $\omega_{T1}=67.42$  meV,  $\omega_{T2}=48.96$  meV,  $\omega_{T3}=35.94$  meV and  $\omega_{T4}=29.50$  meV.  $\gamma_{ph}=0.2$  meV has been taken for both LSCO and YBCO. The values of  $\omega_p$ ,  $\omega_g$ ,  $\delta_{ab}$  and  $\lambda_{ab}$  are chosen to reproduce experimentally measured values of  $\rho_c/\rho_{ab}$ , using Eq. (2.26). Also, value of  $\omega_p$  is consistent with reported experimental value of plasma frequency in LSCO and YBCO [29].

### 2.4.1 Macroscopic Conductivity

Macroscopic conductivity for CS consisting of two 2DCP per unit cell is given by Eqs. (2.15) and (2.17) for longitudinal and transverse field, respectively. Both  $\sigma_{2L}^0$  and  $\sigma_{2T}^0$  are contributed by intralayer as well as interlayer interactions. The contribution of interlayer interactions is given by the second term inside the square bracket on right hand side of Eq. (2.15) and (2.17). For  $k_z \rightarrow 0$ , contribution of interlayer interactions is roughly proportional to  $q^2$  for  $\omega$  close to zero and it is almost zero at higher  $\omega$ -values for all  $q$ -values. It is found that the maximum contribution from interlayer interactions is less than 6% of intralayer interactions for long wavelength case. The macroscopic  $a$ - $b$  plane conductivity for LSCO,  $\sigma_{1ab}^0(q, \omega, T)$  and for YBCO,  $\sigma_{2ab}^0(q, \omega, T)$

are obtained from Eqs. (2.10) and (2.15), respectively on substituting Eq. (2.27) in (2.14) and (2.15) and then taking  $k_z \rightarrow 0$  limit. Our computed  $\text{Re}\sigma_{1ab}^0(q, \omega, T)$ , real part of  $\sigma_{1ab}^0(q, \omega, T)$ , is plotted as function of  $\omega$  for  $qd=0.005$ , in Fig. 2.1 for three different value of  $T$ . As can be seen from the figure, increase in temperature decreases  $\text{Re}\sigma_{1ab}^0(q, \omega, T)$  in lower range of  $\omega$  ( $\omega < \lambda_{ab}T$ ), whereas  $\text{Re}\sigma_{1ab}^0(q, \omega, T)$  increases with  $T$  in middle range of  $\omega$  and then it become independent of  $T$  for  $\lambda_{ab}T \ll \omega$ . The variation of  $\text{Re}\sigma_{1ab}^0(q, \omega, T)$  versus  $T$  at  $qd=0.005$  for two values of  $\omega$  (10 meV and 60 meV) is shown in inset of Fig. 2.1. As is seen,  $\text{Re}\sigma_{1ab}^0$  is approximately proportional to  $1/T$  for  $\omega=10$  meV. It is an expected behavior of  $\text{Re}\sigma_{1ab}^0$  because of linear  $T$ -dependence of  $\rho_{ab}$ . However, at  $\omega=60$  meV,  $\text{Re}\sigma_{1ab}^0$  shows a broad peak located in the range of  $T$ -value, where  $\lambda_{ab}T$  is comparable with  $\omega$ . The peak resembles with the experimentally observed peak in macroscopic conductivity as a function of  $T$  below  $T_c$ , in YBCO at given  $\omega$ -value in microscopic frequency regime.

Our computed  $\text{Re}\sigma_{2ab}^0(q, \omega, T)$  is plotted as a function of  $\omega$  at  $qd=0.005$  for three different values of  $T$ . The general behavior of  $\text{Re}\sigma_{2ab}^0(q, \omega, T)$  versus  $\omega$  is similar to that of  $\text{Re}\sigma_{1ab}^0(q, \omega, T)$ . The over all nature of our computed  $\text{Re}\sigma_{2ab}^0(q, \omega, T)$  as a function of  $\omega$  at different temperatures agrees with the experimentally measured real part of macroscopic conductivity as a function of  $\omega$  at different  $T$  [30]. This supports our choice of  $\gamma$  given by Eq. (2.21). A small peak near about 35.85 meV can be seen in Fig. 2.1 and 2.2. This peak belongs to phonon modes which are incorporated in our calculation through  $\epsilon_l^{ab}(\omega)$ . The plot of our computed  $\text{Re}\sigma_{2ab}^0(q, \omega, T)$  for  $\omega \geq 25$  meV at  $T=100$  K and  $qd=0.005$  along with the experimental data [31] is shown in the inset of Fig. 2.2. As is seen, our computed  $\text{Re}\sigma_{2ab}^0(q, \omega, T)$  shows very good agreement with experimental data for  $25 \text{ meV} \leq \omega \leq 60 \text{ meV}$ . The experimental data also show a

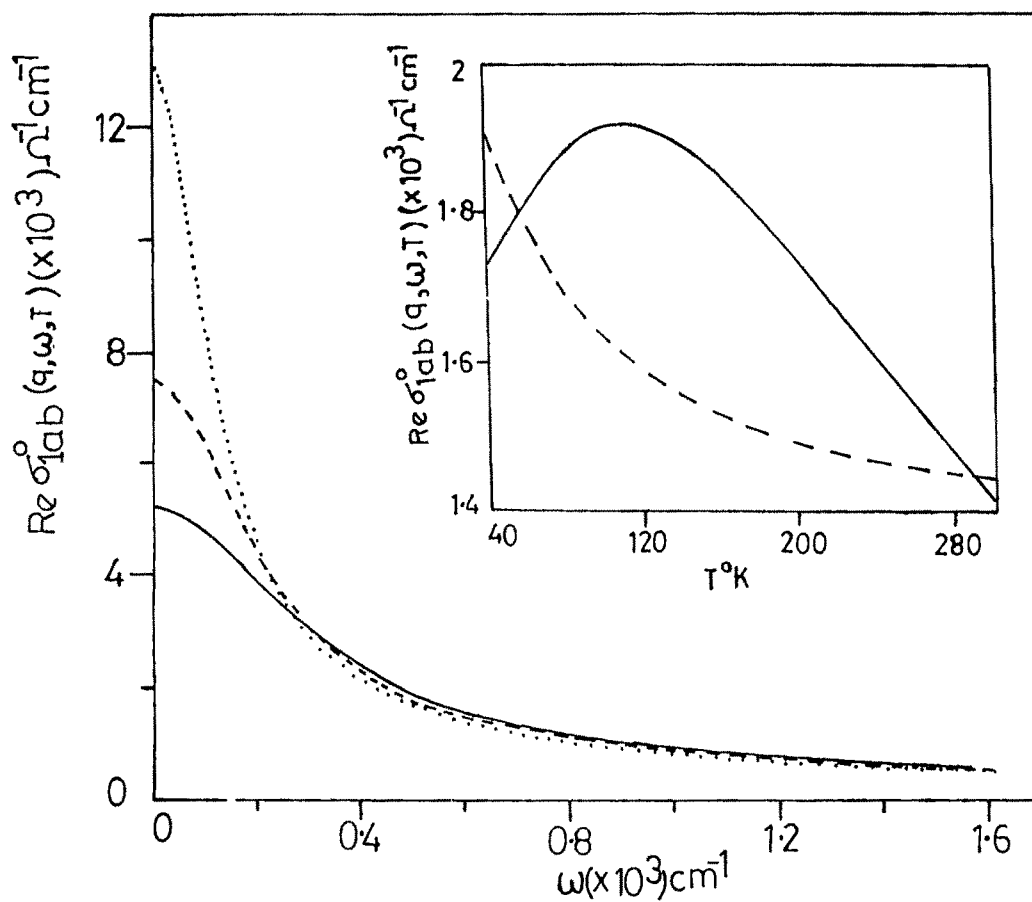


**Fig. 2.1** Plot of  $\text{Re } \sigma_{lab}^0(q, \omega, T)$  as a function of  $\omega$  for  $T=40 \text{ K}$  (dot-dot curve),  $T=70 \text{ K}$  (dash-dash curve) and  $T=100 \text{ K}$  (solid line curve) at  $qd=0.005$ . Inset shows plot of  $\text{Re } \sigma_{lab}^0(q, \omega, T)$  as a function of  $T$  for  $\omega=10 \text{ meV}$  (dash-dash curve) and  $\omega=60 \text{ meV}$  (solid line curve) at  $qd=0.005$ .

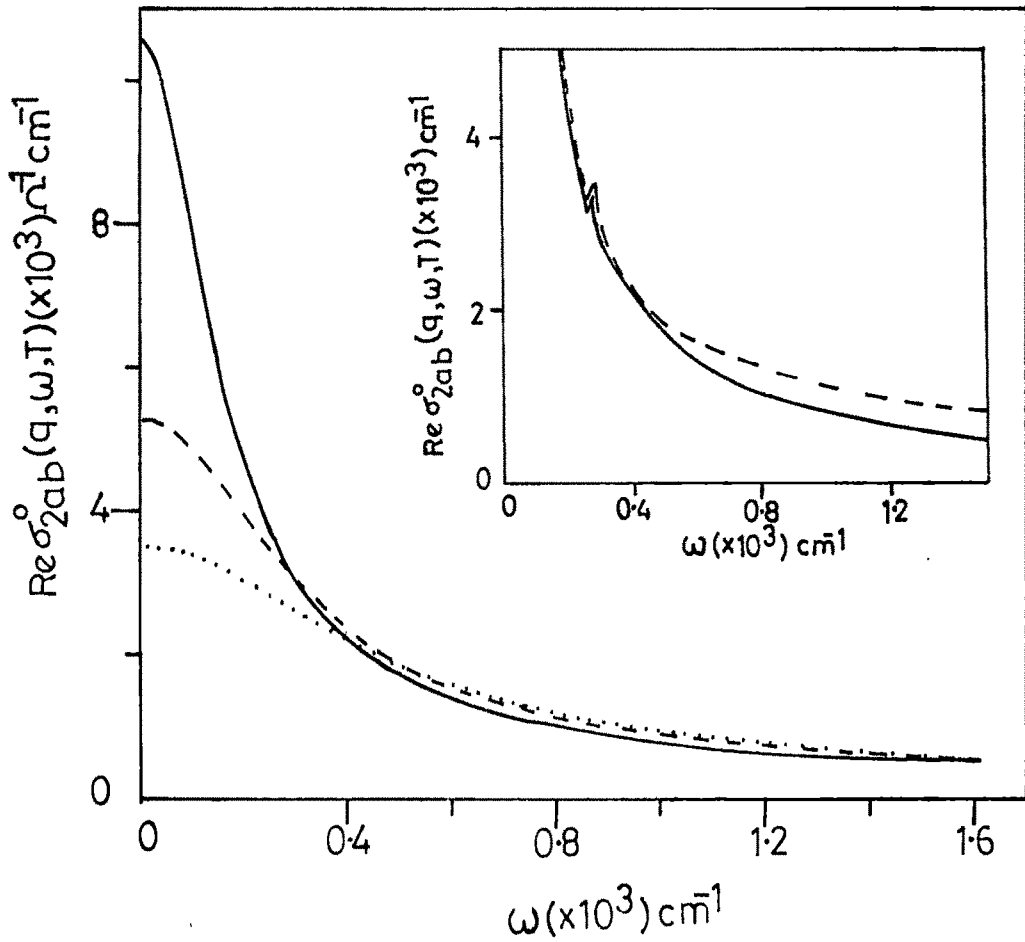
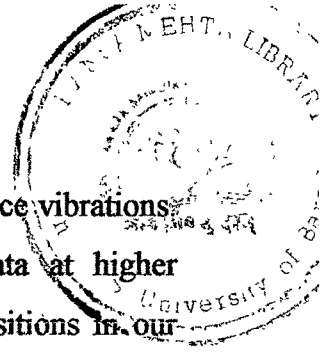


**Fig. 2.2**  $\text{Re } \sigma_{2ab}^0(q, \omega, T)$  is plotted as a function of  $\omega$  at  $qd=0.005$  for  $T=100$  K (solid line curve),  $T=200$  K (desh-desh curve) and  $T=300$  K (dot-dot curve). Comparison of our computed  $\text{Re } \sigma_{2ab}^0(q, \omega, T)$  at  $qd=0.005$  and  $T=100$  K with experimental results (desh-desh curve) is shown in the inset.



small peak for  $\omega$  close to 30 meV, which we believe as due to lattice vibrations. The discrepancy between our calculation and experimental data at higher  $\omega$ -values ( $\omega \geq 60$  meV) is because of exclusion of interband transitions in our calculation. As has been pointed out, interband transition significantly contribute to  $\omega$ -dependent conductivity at higher frequency [16]. Our computation of  $\text{Re}\sigma_{2ab}^0(\mathbf{q}, \omega, T)$  as a function of  $\omega$  for different  $\mathbf{q}$ -values at a fixed  $T$ -value shows that  $\text{Re}\sigma_{2ab}^0(\mathbf{q}, \omega, T)$  decreases on increasing  $\mathbf{q}$  at all  $\omega$ -values.

### 2.4.2 Microscopic Conductivity

The  $a$ - $b$  plane microscopic conductivity is obtained by taking  $k_z \rightarrow 0$  limit of Eq. (2.8) and (2.9).  $\sigma_{mL}(\mathbf{q}, \omega, T)$ , where  $m$  takes value 1 and 2 describes optical conductivity in  $a$ - $b$  plane when  $qd \ll 1$ . We find that for  $\omega < \omega_p$ ,  $\sigma_{mT}(\mathbf{q}, \omega, T) \cong \sigma_{mT}^0(\mathbf{q}, \omega, T)$ , whereas  $\sigma_{mL}(\mathbf{q}, \omega, T) \ll \sigma_{mL}^0(\mathbf{q}, \omega, T)$ . This is because of the severe screening of longitudinal component of field and no screening of transverse component of field for  $\omega < \omega_p$ . The propagation of plasma oscillations (also known as transverse magnetic TM modes) in  $a$ - $b$  plane are studied by calculating complex zeros of  $\epsilon_m(\mathbf{q}, \omega, T)$ . Whereas, propagation of transverse electric (TE) modes in  $a$ - $b$  plane studied by calculating complex zeros of  $F_m(\mathbf{q}, \omega, T)$ . The solution of the  $\epsilon_1(\mathbf{q}, \omega, T) = 0$ , when  $\omega$  is much larger than any of  $\omega_{Li}(\omega_{Ti})$  and it is comparable with  $\omega_p$ , gives

$$\omega_{1p}^{ab}(\mathbf{q}, T) = \left[ \frac{2\omega_0^2 - (\delta_{ab}\beta_{ab})^2 \pm 2i\delta_{ab}\{\omega_0^2(\omega_0^2 + \beta_{ab}^2) + \delta_{ab}^2(\beta_{ab}^4/4)\}^{1/2}}{2(1 + \delta_{ab}^2)} \right]^{1/2}, \quad (2.28)$$

where

$$\omega_0^2 = \frac{\omega_p^2(qd) \sinh(qd)}{2\varepsilon_\infty \cosh(qd) - 1} \quad (2.29)$$

For  $qd \ll 1$ ,  $\omega_0 \cong \omega_p / \sqrt{\varepsilon_\infty}$ , which is much larger than  $\delta_{ab}\beta_{ab}$  when  $T < 100$  K,  $\omega_{1p}^{ab}(q)$  can be simplified to

$$\omega_{1p}^{ab}(q) = \omega_0 [1 + i\delta_{ab}]^{1/2} / [1 + \delta_{ab}^2]^{1/2} \quad (2.30)$$

The  $\text{Re}\omega_{1p}^{ab}(q)$  gives the real part of frequency of plasma oscillations, whereas  $-\text{Im}\omega_{1p}^{ab}(q)$ , imaginary part of frequency of plasma oscillations, is the measure of damping of plasma oscillations. As is obvious from Eq. (2.28),  $-\text{Im}\omega_{1p}^{ab}(q)$  is not very small, as compared to  $\text{Re}\omega_{1p}^{ab}(q)$ , it is 27% of  $\text{Re}\omega_{1p}^{ab}(q)$  for  $\delta_{ab}=0.55$  and  $\beta_{ab}=32.0$ . This results in a broad peak in  $\text{Re}\sigma_{IL}(q, \omega, T)$ . It is important to notice that  $\omega$ - and  $T$ -dependence of  $\gamma_{ab}$  and above mentioned values of  $\delta_{ab}$  and  $\beta_{ab}$  are needed to explain experimentally observed behavior of normal state macroscopic conductivity as a function of  $\omega$  and  $T$ , within our formalism. Further, we relate  $\delta_{ab}$  and  $\lambda_{ab}$  to electron-electron interactions in our model calculation. We therefore can conclude that larger value of  $-\text{Im}\omega_{1p}^{ab}(q)$  is manifestation of electron-electron interactions.  $-\text{Im}\omega_{1p}^{ab}/[\text{Re}\omega_{1p}^{ab}]$  increases on increasing  $T$  and it can approach unity at very high temperatures, as can be seen from Eq. (2.28). This suggests that at very high temperatures plasma oscillations may not remain well behaved and the peak in  $-\text{Im}[1/\varepsilon_1(q, \omega, T)]$  will disappear. Our computed  $-\text{Im}[1/\varepsilon_1(q, \omega, T)]$  is plotted as a function of  $\omega$  at  $qd=0.005$  for three values of  $T$  (40 K, 70 K and 100 K) in Fig. 2.3. As is seen, peak position in  $-\text{Im}[1/\varepsilon_1(q, \omega, T)]$ , which appears at  $\omega=\text{Re}\omega_{1p}^{ab}$ , remains almost unchanged. However, peak height decreases marginally on increasing  $T$ . Peaks

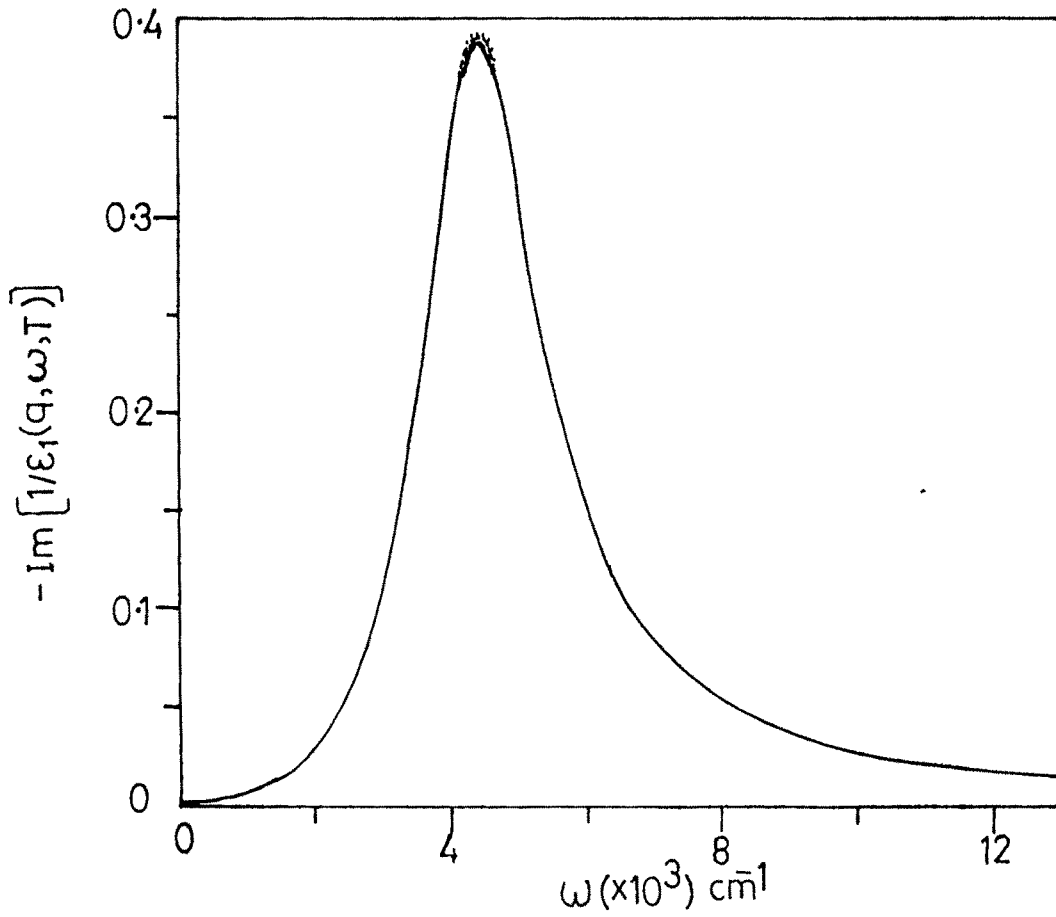


**Fig. 2.3** Plot of  $-\text{Im}[1/\epsilon_1(q, \omega, T)]$  as a function of  $\omega$  at  $qd=0.005$  for  $T=40$  K (dot-dot curve),  $T=70$  K (desh-desh curve) and  $T=100$  K (solid line curve). Three curves are distinguishable near about the peak.

which correspond to phonon frequencies are not seen here because of their suppression due to the screening of longitudinal component of field. In order to see how plasma oscillations in CS like YBCO differ from those in CS like LSCO, we solve  $\epsilon_2(q, \omega, T) = 0$  for  $qd \ll 1$  when  $\epsilon_l(\omega)$  is replaced by  $\epsilon_\infty$ . We obtained two values of  $\omega$  for which  $\epsilon_2(q, \omega, T) = 0$  is satisfied,

$$\omega_{2p}^+(q, T) = \left[ \frac{4\omega_p^2 - (\delta_{ab}\beta_{ab})^2 \pm 2i\delta_{ab}\{4\omega_p^4 + 2\omega_p^2\beta_{ab}^2 - \delta_{ab}^2\beta_{ab}^4/4\}^{1/2}}{2(1 + \delta_{ab}^2)} \right]^{1/2}, \quad (2.31)$$

$$\omega_{2p}^-(q, T) = \left[ \frac{2Z^2 - (\delta_{ab}\beta_{ab})^2 \pm 2i\delta_{ab}\{Z^4 + Z^2\beta_{ab}^2 - \delta_{ab}^2\beta_{ab}^4/4\}^{1/2}}{2(1 + \delta_{ab}^2)} \right]^{1/2}, \quad (2.32)$$

where  $Z=(qd\omega_p/3)$ .  $\omega_{2p}^+(q)$  behaves like  $\omega_{1p}^{ab}(q)$  except that the magnitude of real and imaginary parts of  $\omega_{2p}^+(q)$  are larger than those of  $\omega_{1p}^{ab}(q)$ . We again find that imaginary part of  $\omega_{2p}^+(q)$  is approximately 27% of its real part, as  $\delta_{ab}$  is taken 0.55 for both LSCO and YBCO. The  $\omega_{2p}^-(q)$  is caused by interlayer interactions in YBCO, which has two 2DCP layer per unit cell. An interesting information is provided by Eq. (2.32). As can be seen,  $\omega_{2p}^-(q)$  has non-zero real part for  $Z \geq \delta_{ab}\beta_{ab}$ , which suggests that there exists a cut-off  $q$ -values,  $q_c=(3\delta_{ab}\beta_{ab}/\omega_p d)$ . For  $q < q_c$ , plasma mode of frequency  $\omega_{2p}^-(q)$  does not propagate. We further find that for  $q > q_c$ ,  $\omega_{2p}^-(q)$  is roughly proportional to  $(q^2 - q_c^2)^{1/2}$ . This further suggests that there is no possibility of observing soft acoustic plasma modes in any of CS as has been observed in several experiments performed to measure plasmons in normal state of CS. With the use

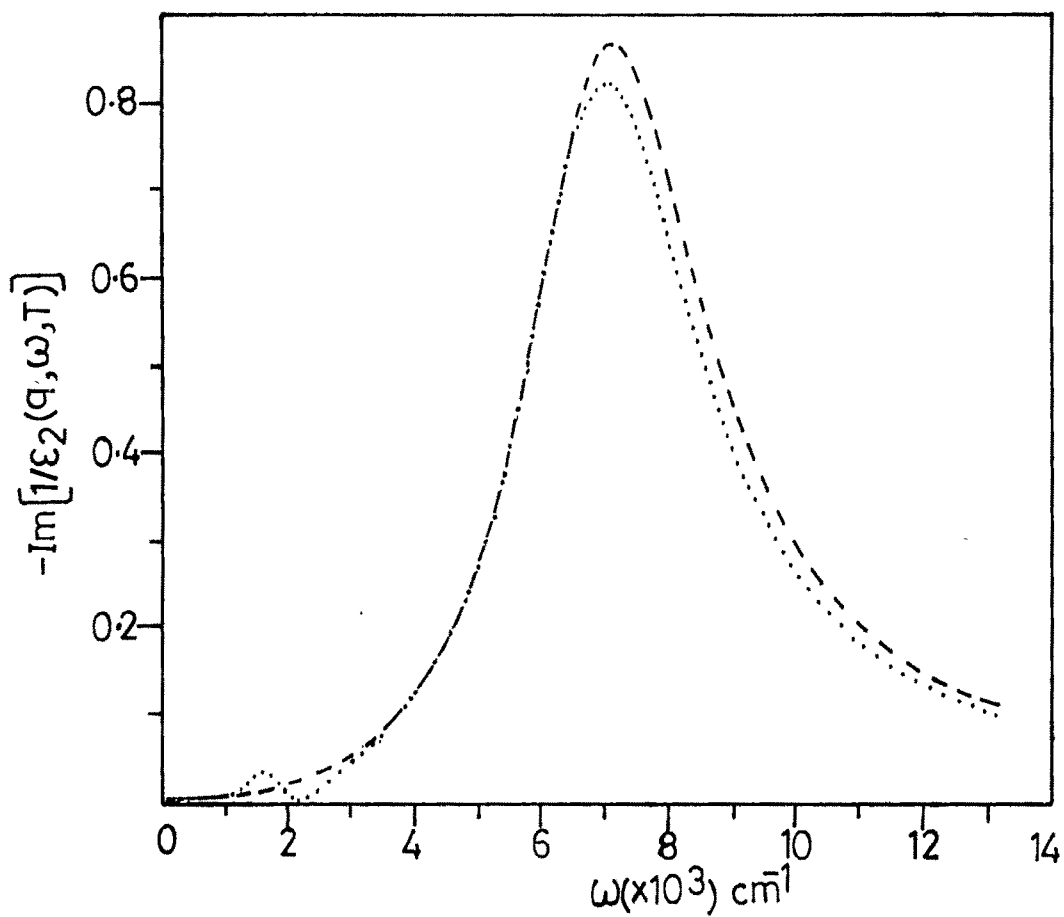
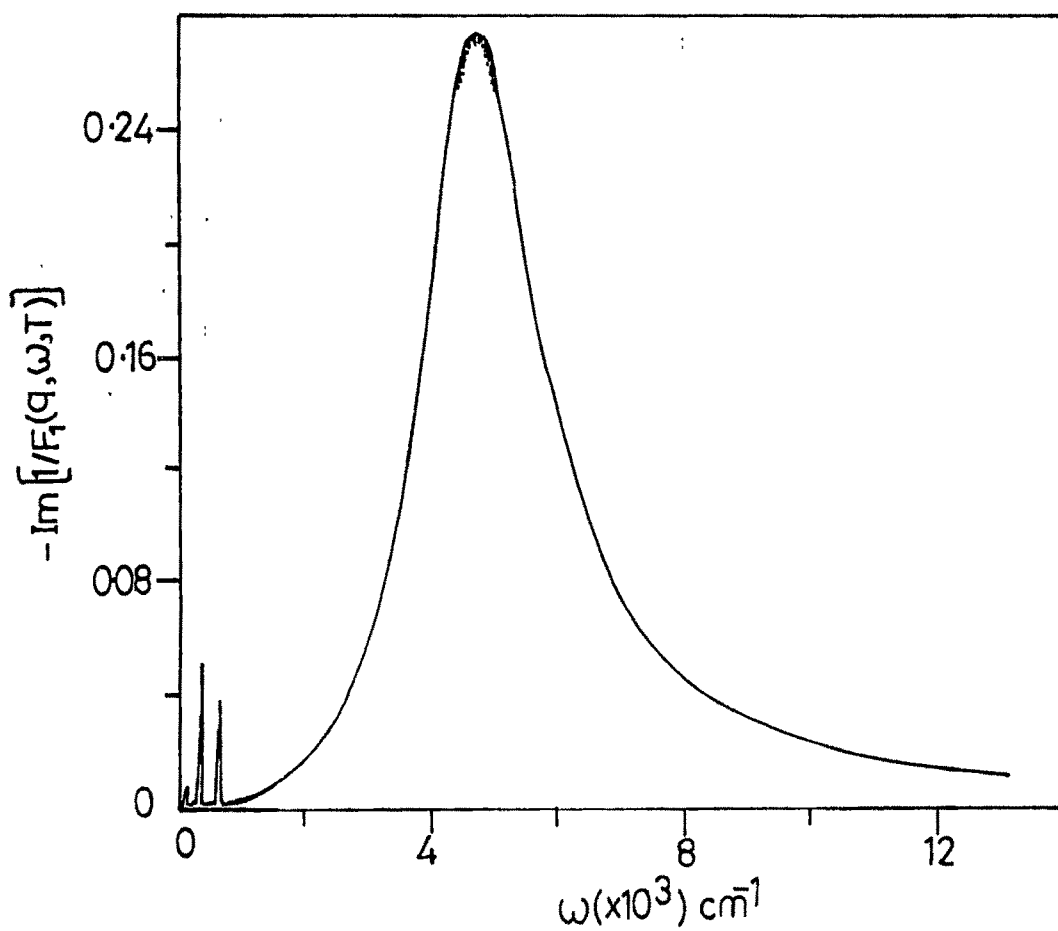


Fig. 2.4 Plot of  $-\text{Im}[1/\epsilon_2(q, \omega, T)]$  as a function of  $\omega$  at  $T=100$  K for  $qd=0.005$  and  $0.1$  (desh-desh curve) and  $qd=1.0$  (dot-dot curve). Two curves of  $-\text{Im}[1/\epsilon_2(q, \omega, T)]$  for  $qd=0.005$  and  $0.1$  merges with each other.



**Fig. 2.5** Plot of  $-\text{Im}[1/F_1(q, \omega, T)]$  as a function of  $\omega$  at  $qd=0.005$  for three values of  $T$  (40 K, 70 K and 100 K). Three curves merge with each other for all values of  $\omega$  except  $\omega$  close to peak position. Peak height increasing with increase in temperature.

$-\text{Im}[1/\epsilon_1(q, \omega, T)]$ ,  $-\text{Im}[1/F_1(q, \omega, T)]$  exhibits sharp small peaks in low frequency regimes, which belong to phonon modes. The peaks representing phonons are seen in Fig. 2.5 because of almost no screening of transverse field for  $\omega < \omega_p$ .

Solution of  $F_2(q, \omega, T) = 0$  for  $\omega$  as a function of  $q$  and  $T$  gives complex frequency of TE modes which can propagate in normal state of YBCO. Again, like the case of LSCO, there exist large number of TE modes in YBCO. Unlike the case of TM modes, there does not exist any TE mode in YBCO whose frequency goes to zero at  $q=q_c$ . Real and imaginary parts of frequency of a TE mode, which has smallest frequency,  $\omega_{2t}^s(q)$  among all TE modes existing in a CS like YBCO, are plotted as a function of  $q$  in Fig. 2.6 at  $T=100$  K. As can be notice from the figure, both  $\text{Re}\omega_{2t}^s(q)$  and  $\text{Im}\omega_{2t}^s(q)$  vary almost linearly with  $q$  and  $\{\text{Im}\omega_{2t}^s(q)/\text{Re}\omega_{2t}^s(q)\} \cong 26\%$  at all  $q$ -values. For  $q \rightarrow 0$ ,  $\omega_{2t}^s(q)$ , can approximately be given by

$$\omega_{2t}^s(q) \cong \omega_p \{2(1+i\delta_{ab}) / (2\epsilon_\infty - 1)(1+\delta_{ab}^2)\}^{1/2}. \quad (2.33)$$

For  $qd < 0.001$ , both  $\text{Re}\omega_{2t}^s(q)$  and  $\text{Im}\omega_{2t}^s(q)$  become almost independent of  $q$ , as is seen in inset of Fig. 2.6. Other TE modes exist at very high  $\omega$ -values. The real part of the frequency of next TE mode in YBCO is approximately equal to 286.15 eV.

## 2.5 CONDUCTIVITY ALONG $c$ -AXIS

The  $c$ -axis conductivities are calculated by substituting Eqs. (2.20) and (2.21) into Eqs. (2.10) and (2.15) and then taking  $q \rightarrow 0$  limit of Eqs. (2.8) to (2.19). Eq. (2.20) for  $q \rightarrow 0$ , reduces to

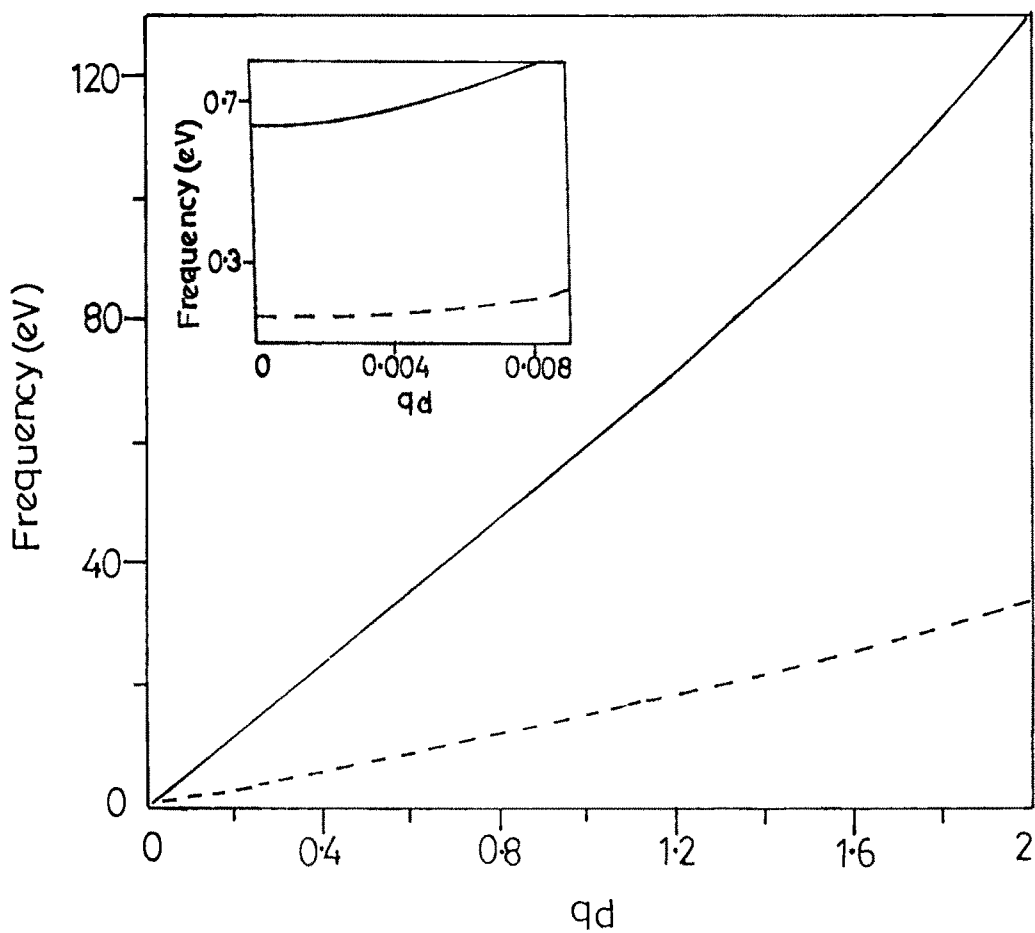


**Fig. 2.6** Real part (solid line curve) and imaginary part (desh-desh curve) of  $\omega_{2p}^+(q, T)$  and  $\omega_{2p}^-(q, T)$  are plotted as a function of  $qd$  at  $T=100$  K. Inset shows the curves for  $qd \rightarrow 0$ .

$$\alpha^c(k_z, \omega, T) = \frac{\omega_g^2 \sin^2(k_z d/2)}{\pi e^2 d^2 \omega (\omega + i\gamma)} \quad (2.34)$$

$\gamma_c$  is given by Eq. (2.21) on replacing  $\delta$  by  $\delta_c$  and  $\beta$  by  $\lambda_c/T$ . We take  $\delta_c = 0.11$  and  $\lambda_c = 1280$  meV K for LSCO and  $\delta_c = 0.11$  and  $\lambda_c = 4000$  meV K for YBCO. Values of phonon frequencies to compute  $\epsilon_l(\omega)$  along  $c$ -axis,  $\epsilon_l^c(\omega)$ , are taken to be  $\omega_{L1} = 52.43$  meV,  $\omega_{L2} = 25.78$  meV,  $\omega_{L3} = 18.59$  meV,  $\omega_{T1} = 46.48$  meV,  $\omega_{T2} = 19.95$  meV,  $\omega_{T3} = 13.50$  meV for YBCO and  $\omega_{L1} = 76.74$  meV,  $\omega_{L2} = 57.63$  meV,  $\omega_{T1} = 61.22$  meV,  $\omega_{T2} = 30.00$  meV for LSCO [24]. The  $\epsilon_l^c(\omega)$  is needed to calculate macroscopic and microscopic conductivity along  $c$ -axis.

### 2.5.1 Macroscopic Conductivity

The  $c$ -axis macroscopic conductivity is given by Eq. (2.10) for LSCO and by Eq. (2.15) for YBCO on taking  $q \rightarrow 0$  limit and by making use of Eq. (2.34). The  $c$ -axis macroscopic conductivity for LSCO,  $\sigma_{1c}^0(\omega, T)$  is found independent of  $k_z$ , whereas that of YBCO,  $\sigma_{2c}^0(k_z, \omega, T)$  depends on  $k_z$ . Our computed  $\text{Re}\sigma_{1c}^0(\omega, T)$  is plotted as a function of  $\omega$  in Fig. 2.7 for three values of  $T$  (40 K, 70 K and 100 K). Like the case of  $\text{Re}\sigma_{1ab}^0(q, \omega, T)$ ,  $\text{Re}\sigma_{1c}^0(\omega, T)$  decreases on increasing  $\omega$  for  $\omega$  not close to phonon frequency, as can be seen from the figure. However,  $\text{Re}\sigma_{1c}^0(\omega, T)$  shows: (i) linear  $T$ -dependence for  $\omega$  close to zero, (ii) magnitude of  $\text{Re}\sigma_{1c}^0(\omega, T)$  is smaller than that of  $\text{Re}\sigma_{1ab}^0(q, \omega, T)$  for  $\omega$  smaller than phonon frequency and (iii) large height peaks which correspond to lattice vibrations, because of  $\gamma_c < \gamma_{ab}$ . The behavior of  $\text{Re}\sigma_{1c}^0(\omega, T)$  with  $T$  at  $\omega = 1.0$  meV and at  $\omega = 8.0$  meV found similar to that of  $\text{Re}\sigma_{1ab}^0(q, \omega, T)$  versus  $T$  at  $\omega = 60.0$  meV and  $\omega = 10.0$  meV, respectively. This can be understood in terms of  $T$ -dependence of  $\rho_c$  and  $\rho_{ab}$ . The behavior of our computed

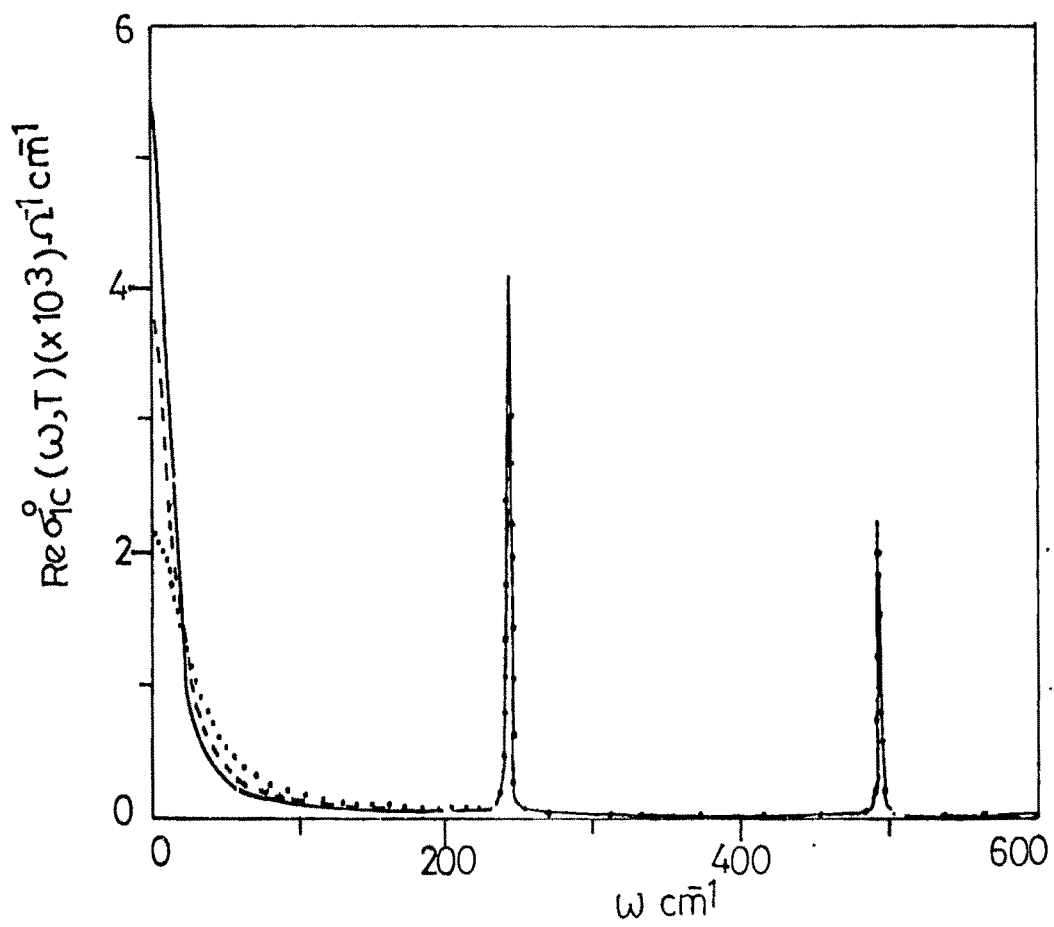


Fig. 2.7 Plot of  $\text{Re } \sigma_{1c}^0(\omega, T)$  as a function of  $\omega$  for  $T=40$  K (dot-dot curve),  $T=70$  K (dash-dash curve) and  $T=100$  K (solid line curve).

$\text{Re}\sigma_{2c}^0(k_z, \omega, T)$  versus  $\omega$  and  $T$  at given  $k_z$  value is found similar to that of  $\text{Re}\sigma_{1c}^0(\omega, T)$  with  $\omega$  and  $T$ .

### 2.5.2 Microscopic Conductivity

The microscopic conductivity along  $c$ -axis is obtained from Eqs. (2.10) and (2.15) by taking  $q \rightarrow 0$  limit. As is obvious, a transverse field can not be confined to a single direction,  $c$ -axis conductivity can therefore not defined. Therefore, we computed,  $\sigma_{1L}^0(\omega, T)$  and  $\sigma_{2L}^0(k_z, \omega, T)$ ,  $c$ -axis microscopic conductivity for CS like LSCO and YBCO, respectively.  $\sigma_{1L}^0(\omega, T)$  is independent of  $k_z$ , whereas  $\sigma_{2L}^0(k_z, \omega, T)$  depends on  $k_z$  because of contribution of interlayer interactions to  $\sigma_{2L}^0(k_z, \omega, T)$ . Similar to the case of  $\epsilon_2(q, \omega, T)$ , we obtained two plasma frequency on solving  $\epsilon_2(k_z, \omega, T)=0$  for  $\omega$  as a function of  $k_z$ . Frequency of lower plasma mode is approximately given by Eq. (2.32) on replacing  $\delta_{ab}$  and  $\beta_{ab}$  by  $\delta_c$  and  $\beta_c$ , respectively and then taking

$$Z^2 = \omega_g^2 / \epsilon_\infty [1 - \{1 - 8\sin^2(k_z d/2)/9\}^{1/2}] \quad (2.35).$$

This suggests that lower  $c$ -axis plasma mode can exist for  $k_z \geq k_{zc}$ , where

$$k_{zc} = \{2/d\} \sin^{-1} [9/8 \{2\delta_c^2 \beta_c^2 \epsilon_\infty / \omega_g^2 - (\delta_c^2 \beta_c^2 \epsilon_\infty / \omega_g^2)^2\}]^{1/2} \quad (2.36).$$

On substituting values of  $\delta_c$ ,  $\beta_c$ ,  $\epsilon_\infty$  and  $\omega_g$ , we find that lower  $c$ -axis plasma frequency is non-zero for  $k_z d \geq 0.11$ . Our computed  $\text{Re}\sigma_{2L}^0(k_z, \omega, T)$  as a function of  $\omega$  is plotted in Fig. 2.8, for  $k_z d = 0.005, 0.1$  and  $1.0$  at  $T = 100$  K. Large and broad peak represents the upper  $c$ -axis plasma mode, whereas one of the small peaks in low frequency regime ( $\omega \leq 500 \text{ cm}^{-1}$ ) belong to lower  $c$ -axis plasma mode. Other small peaks in low frequency regime belong to lattice

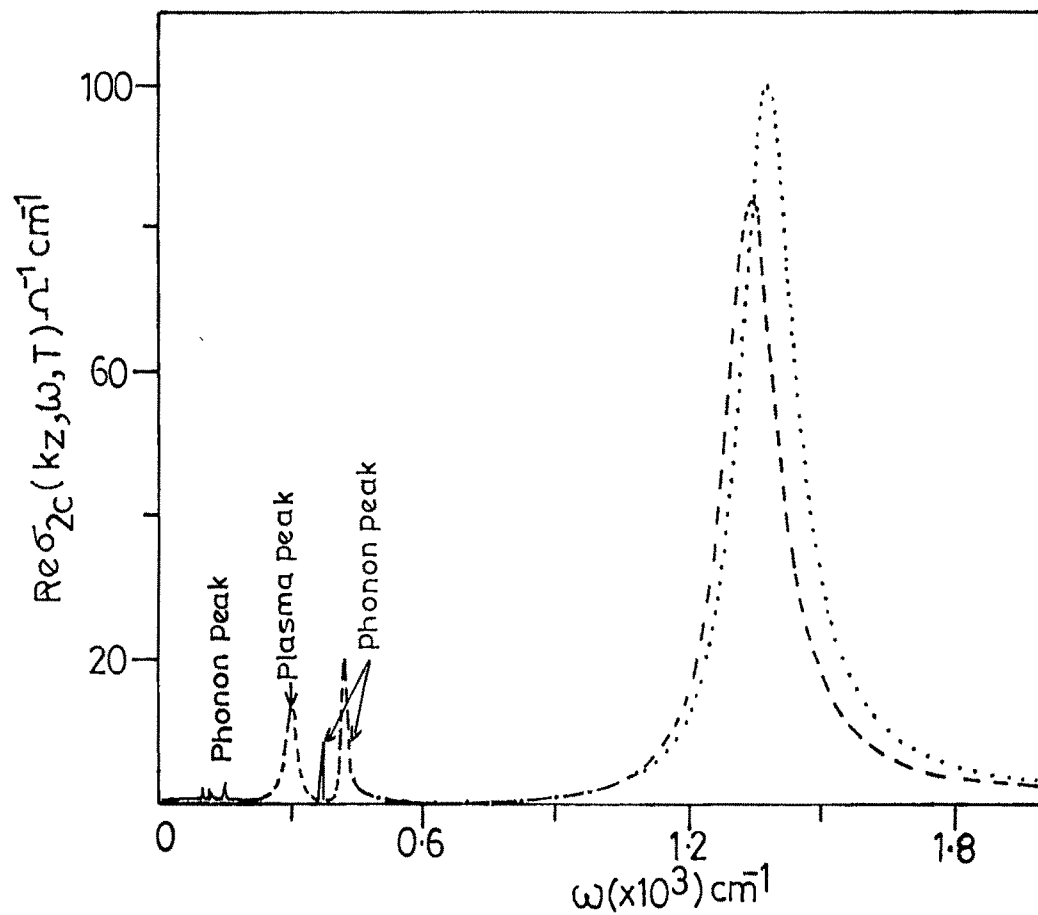


**Fig. 2.8** Plot of  $\text{Re } \sigma_{2c}(k_z, \omega, T)$  as a function of  $\omega$  at  $T=100$  K for  $k_z d=0.005$  and  $0.1$  (dot-dot curve) and  $k_z d=1.0$  (dash-dash curve). Two curves of  $\text{Re } \sigma_{2c}(k_z, \omega, T)$  for  $k_z d=0.005$  and  $0.1$  merge with each other.

vibration modes, which propagate along  $c$ -axis. The peak at around  $\omega = 317.23 \text{ cm}^{-1}$  represents lower  $c$ -axis plasma mode at  $k_z d = 1.0$ . Position of peak, representing lower plasma mode, shifts towards higher  $\omega$ -value and its size increases on increasing  $k_z d$ . Whereas, size of peak representing upper plasma mode, reduces and its position shifts towards lower  $\omega$ -value on increasing  $k_z d$ . Existence of a broad peak in  $c$ -axis optical conductivity at around  $\omega = 100 \text{ meV}$  has also been shown by Atkinson and Carbotte [10] in their calculation of normal state  $c$ -axis optical conductivity of YBCO. As is obvious, broad peak in our computed  $\text{Re}\sigma_{2L}^c(k_z, \omega, T)$  is originated from charge transfer along  $c$ -axis which is represented by  $\omega_g$  and the  $\omega$ -and- $T$ -dependent  $\rho_c$ . Our simple model calculation qualitatively agrees with detail numerical calculation of  $c$ -axis optical conductivity of Atkinson and Carbotte [10]. It can therefore be said that our simple model calculation qualitatively described broad feature of normal state dynamical conductivity of a CS

## REFERENCES

- [1]. W. E. Pickett, **Rev. Mod. Phys.** **61** (1989), 433 and references therein.
- [2]. C. C. Homes, T. Timusk, R. Liang, D. A. Bonn and W. N. Hardy,  
**Phy. Rev. Lett.** **71** (1993), 1645; C. C. Homes, T. Timusk, D. A. Bonn, R.  
Liang, and W. N. Hardy, **Physica C265** (1995).
- [3]. J. Schutzmann, S. Tajima, S. Miyamoto and S. Tanaka, **Phy. Rev. Lett.** **73**  
(1994), 174.
- [4]. Y. Zha, S. L. Cooper and D. pines, **Phy. Rev.** **B53** (1996), 8253.
- [5]. M. J. Graf, D. Rainer and J. A. Sauls, **Phy. Rev.** **B47** (1993), 12089.
- [6]. H. Kitano, T. Hanaguri and A. Maeda, **Phy.Rev.** **B57** (1998),10946.
- [7]. A. G. Rojo and K. Levin, **Phy. Rev.** **B48** (1993), 1686.
- [8]. A. J. Leggett, **Braz. J. Phys.** **22** (1992), 129.
- [9]. N. Kumar and A. M. Jayannavar, **Phy. Rev.** **B45** (1992), 5001.
- [10]. W. A. Atkinson and J. P. Carbotte, **Phy. Rev. B** **55** (1997), 12748.
- [11]. W. A. Atkinson and J. P. Carbotte, **Phy. Rev.** **B52** (1995), 10601.
- [12]. H. Ding, M.R. Norman, T. Yokoya, T. Takeuchi, M. Randeria,  
J. C. Campuzano, T. Takahashi, T. Mochiku and K. Kndowaki,  
**Phy.Rev. Lett.** **78** (1997), 2628.
- [13]. J. Demsar, M. Zavrtanik and B. Podovmik, V.I. Dediú and D. Mihalovie,  
**J. Supercond.** **10** (1997), 455.
- [14]. A. V. Puchkov, P. Fourniem, D. N. Basov, T. Timusk, A. Kapitulnik and  
N. Kalesinkov, **Phy. Rev. Lett.** **77** (1996),3212.
- [15]. A. V. Puchkov, D. N. Basov and T. Timusk, **J. Cond. Matt.****8** (1996),  
10049.
- [16]. D. Mihalovie, T. Merteli and K. A. Muller, **Phy. Rev.** **B57** (1996),6116.
- [17]. H. A. Fertig and S. Das Sarma, **Phy. Rev.** **B44** (1991), 4480.
- [18]. Susumu Misawa, **Phy. Rev.** **B53** (1996), 2241.
- [19]. G. D, Mehan and Ji. Wei Wu, **Phy Rev.** **B39** (1989), 265.